Journal of Alloys and Compounds 813 (2020) 152194

Contents lists available at ScienceDirect

Journal of Alloys and Compounds

journal homepage: http://www.elsevier.com/locate/jalcom

Review

Structural, photoluminescent properties and Judd-Ofelt analysis of Eu^{3+}-activated CaF_2 nanocubes

Eugenio Cantelar [a, *], Juan Antonio Sanz-García [a], Adrián Sanz-Martín [a], Juan Enrique Muñoz Santiuste [b], Fernando Cussó [a]

[a] Departamento de Física de Materiales, C-04, Facultad de Ciencias, Universidad Autónoma de Madrid, 28049, Madrid, Spain
[b] Departamento de Física, Escuela Politécnica Superior, Universidad Carlos III de Madrid, 28911, Leganés, Madrid, Spain

ARTICLE INFO

Article history:
Received 23 May 2019
Received in revised form
5 September 2019
Accepted 6 September 2019
Available online 6 September 2019

Keywords:
CaF_2 nanoparticles
Eu^{3+}
Rietveld refinement
Judd-Ofelt
Concentration dependence

ABSTRACT

Eu^{3+}-doped CaF_2 nanocubes with variable europium concentration, $[Eu^{3+}] = 0$, 0.6, 1.3, 1.7, 2.2 and 5.4 mol%, have been synthesized by a direct precipitation route. It has been found that, within this concentration range, the nanoparticles present the fluoride-type crystalline structure and the characteristic cubic shape of CaF_2 crystals. The nanoparticle size follows a log-normal distribution with a mean value decreasing with the Eu^{3+} content. Rietveld refinement has been performed to calculate the lattice parameter and crystallite size. Eu^{3+} concentration affects both parameters giving rise to an increase in the lattice parameter and a reduction of crystallite size. The luminescent properties of Eu^{3+} ions in these nanostructures have been investigated under CW and pulsed excitation. A Judd-Ofelt analysis, as function of the Eu^{3+} content, has been performed to determine the transition probabilities, radiative lifetimes and branching ratios of the $^5D_0$ emitting level. It was found that Ω_2 and Ω_4 Judd-Ofelt intensity parameters are dependent on the doping level, showing an evolution that indicates a decrease in the Eu^{3+} site local symmetry with increasing Eu^{3+} concentration. Finally, it has been observed that the characteristic luminescence decay time of the $^5D_0$ manifold is reduced with increasing Eu^{3+} concentration. This effect is partially due to an increase of radiative transition probability, associated with a reduction in the local symmetry of the lanthanide ions, and also to the occurrence of concentration quenching effects.

Contents

1. Introduction

There is a crescent interest in lanthanide (Ln^{3+}) doped nanomaterials due to their potential applications in several emerging

* Corresponding author. Avda. Francisco Tomás y Valiente nº 7, Departamento de Física de Materiales, C-04, Facultad de Ciencias, Universidad Autónoma de Madrid, 28049, Madrid, Spain.
E-mail address: eugenio.cantelar@uam.es (E. Cantelar).

https://doi.org/10.1016/j.jallcom.2019.152194

fields of science and technology. In fact, nowadays, it has been demonstrated their capabilities in many areas such as the development of efficient solar cells [1] and white LEDs (wLEDs) [2], luminescent probes for in vivo medical imaging [3] and tumor detection [4], contrast agents in Magnetic Resonance Imaging [5], etc. Most of these applications are based on the capacity that offer Ln^{3+} ions for energy conversion via Stokes and anti-Stokes shift [6].

Of paramount importance are the criteria used to select the combination host and Ln^{3+} ion. In fact, the matrix where the active ions are embedded must satisfy some requirements to ensure the role that Ln^{3+} ions must play in the desired application. Among the different optical nanomaterials, binary and ternary fluorides attract a great deal of interest because of their low phonon energies, high refractive indices, broad transparency window, thermal and chemical stability as well as the possibility of dopant incorporation [7–11]. Between the different binary fluorides, Ln^{3+} activated alkali earth fluorides have been widely investigated over time because these hosts not only gather all these properties, but also because such nanostructures can be synthesized, at low temperatures, by using facile chemical routes based on precipitation techniques [8–11].

CaF_2 NPs activated with Ln^{3+} ions are currently an active research field in order to improve the efficiency of these systems through a better knowledge of their basic properties [9–16]. At variance with other lanthanide ions, Eu^{3+} ions offer a unique combination of intra-configurational 4f → 4f transitions of pure magnetic or electric-dipole character that make them especially sensitive to the chemical local environment. Therefore, Eu^{3+} ions are considered adequate spectroscopic probes to explore the local symmetry when are incorporated into a crystalline host [17,18]. Additionally, Eu^{3+} ions are attractive candidates as energy converters, due to their ability to transform ultraviolet radiation in an intense orange-red emission useful, for example, for wLED applications where red nanophosphors under UV excitation are demanded [2].

Although it is possible to find some works dedicated to the study of the optical properties of Eu^{3+}-activated CaF_2 nanostructures [9–11], the basic spectroscopic properties of Eu^{3+} ions in calcium fluoride NPs are not fully understood. In the present work, Eu^{3+}-doped CaF_2 NPs with variable europium concentration were synthesized by a direct precipitation method at low temperature and pH = 3. X-ray Powder Diffraction and Scanning Electron Microscopy have been used to analyze the crystalline structure and morphology of the NPs. The basic luminescent properties of Eu^{3+} ions have been studied under CW and pulsed excitation. A modified Judd-Ofelt procedure, based on the analysis of the emission spectrum [17,18], has been used to determine the basic luminescent properties of the $^5D_0$ emitting level (transition probabilities, radiative lifetimes and branching ratios) as function of Eu^{3+} concentration. The evolution of the Judd-Ofelt intensity parameters (Ω_2 and Ω_4) is discussed in terms of a local symmetry reduction of Eu^{3+} sites as the doping level increases. Finally, it has been established that the temporal dynamics of the $^5D_0$ manifold is affected by concentration quenching processes.

2. Experimental details

2.1. Synthesis of samples

Eu^{3+}-doped CaF_2 nanoparticles (NPs) with variable europium concentration, ranging from 0 mol% to 5.4 mol%, were prepared by a low temperature direct precipitation method [10,11]. In this synthesis route, $CaCl_2 \cdot 2H_2O$ (99.9%), $EuCl_3 \cdot 6H_2O$ (99.9%) and NH_4F (99.9%), from Alfa Aesar, were used as starting reactants due to their high solubility in water. The solid precipitation of calcium fluoride is produced by the chemical reaction of Ca^{2+} and F^- ions formed by the $CaCl_2$ and NH_4F dissociation in aqueous medium.

The appropriate amount of cationic precursors, $CaCl_2$ and $EuCl_3$ salts, were added to a beaker containing 200 ml of deionized water and the total cationic concentration was controlled to be 0.01 mol/l. Additionally, the pH of this cationic solution was adjusted at pH = 3 by adding 30 mg of hydrochloric acid (36%). The solution was heated till temperature reaches a value close to T = 100 °C. In this moment, a second solution (0.08 mol/l) containing the NH_4F anionic precursor was slowly added to the beaker. The acid pH value was chosen in order to maintain a low enough concentration of fluorine ions in the cationic solution avoiding, therefore, a fast precipitation of the calcium fluoride NPs.

After the precipitation, the precursors were separated from the nanoparticles by centrifugation and subsequent washing with ethanol and deionized water. Then the final product was dried at 60 °C during 24 h and collected for characterization.

Europium concentrations were determined by X-ray fluorescence spectrometry (TXRF) and are summarised in Table 1.

2.2. Characterization techniques

The phase and crystalline structure have been investigated by X-Ray Powder Diffraction (XRD) by using an X'Pert Pro Theta/ 2 Theta diffractometer (Cu K_α radiation, $\lambda = 0.15406$ nm) in a scan range 20–100°. The size and morphology of the nanocrystals have been studied by a Philips XL30 S-FEG Scanning Electron Microscope (SEM).

The photoluminescence characterization, under CW conditions, has been performed by using a conventional single ultraviolet LED, ($\lambda = 401$ nm) from a 3 M LED strip. Lifetime measurements were performed after excitation with the second harmonic of a pulsed Nd:YAG laser ($\lambda = 532$ nm), Spectra Physics model DCR 2/2A 3378, with a pulse width of 10 ns and a repetition rate of 10 Hz. Independently on the pumping scheme, CW or pulsed excitation, the luminescent signal was dispersed by using an ARC monochromator model SpectraPro 500-i and then detected with an EMI-9558QB photomultiplier. Additionally for lifetime measurements, the signal was averaged and recorded by a Tektronix DPO4104B-L digital oscilloscope.

3. Results and discussion

3.1. Structural analysis and morphology

The XRD patterns of the as-prepared CaF_2:Eu^{3+} NPs for the different Eu^{3+} concentrations, together with the pattern expected for calcium fluoride crystal, PDF 04-007-5933 from the International Centre for Diffraction Data (ICDD, 2011), are shown in Fig. 1(a). The diffraction peaks, detected in the range $20° \leq 2\theta \leq 100°$, can be indexed to the fluoride-type structure ($Fm\bar{3}m$ space group). In particular, the observed peaks correspond to the diffraction of (1 1 1), (2 2 0), (3 1 1), (4 0 0), (3 3 1), (4 2 2) and (5 1 1) crystalline planes; which indicates that the synthesized NPs are isostructural with CaF_2 crystal.

On the other hand, the increase of europium concentration give rise to a gradual shift of the diffraction peaks to small angles as well as a clear broadening in the diffraction peak profile, as it is illustrated in Fig. 1(b) for the (2 2 0) crystalline plane. These concentration effects have been previously observed in other lanthanide (Ln^{3+}) doped alkali earth fluorides and they have been attributed to lattice distortion due to the gradual incorporation of interstitial fluorine ions [10,16,19,20]. In the case of Eu^{3+}-doped CaF_2, it has been reported that Eu^{3+} ions are incorporated to the host by substituting the Ca^{2+} ions producing an excess of positive charge.

Table 1
Main structural and morphological parameters of CaF_2:Eu^{3+} NPs with different doping levels.

Sample	[Eu^{3+}] (mol%)	Lattice parameter[a] $a = b = c$ (Å)	Crystallite size (nm)	Mean particle size (nm)	Standard deviation (nm)
# 0	0.0	5.4617	103	79	39
# 1	0.6	5.4637	91	60	31
# 2	1.3	5.4642	58	49	33
# 3	1.7	5.4652	50	41	27
# 4	2.2	5.4661	48	38	33
# 5	5.4	5.4676	42	36	23

[a] Estimated standard deviation value for lattice parameter: 8×10^{-4} Å.

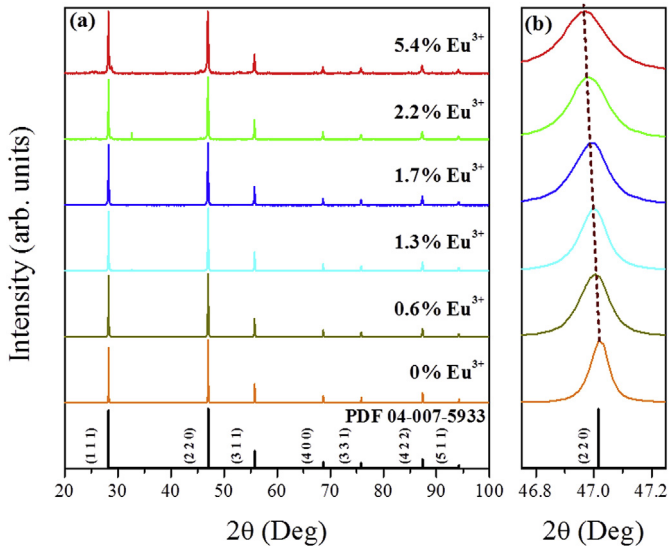

Fig. 1. - (a) XRD patterns of the as-prepared CaF_2:Eu^{3+} nanocrystals as function of Eu^{3+} concentration. (b) Angular shift and broadening of the (2 2 0) diffraction peak.

This extra charge may be compensated by the occurrence of structural defects, in particular by the formation of interstitial fluorine ions according to the charge compensation mechanism: $Ca^{2+} \rightarrow Eu^{3+} + F^{-}$. In general, the progressive angular shift and peak profile broadening with Eu^{3+} concentration are attributed to a parallel increment of interstitial fluorine ions. Therefore, such effects are a clear signature of the Eu^{3+} incorporation to the CaF_2 lattice.

Rietveld refinement has been performed by using the FullProf Suite open access software from the Institut Laue-Langevin in Grenoble (France). As an example, the fitted XRD patterns for the NPs # 0, # 3 and # 5 are presented in Fig. 2. As it has been previously mentioned, the main diffraction peaks can be indexed to the fluoride-type structure ($Fm\bar{3}m$ space group). However, a closer inspection reveals that in the case of the most concentrated sample a very small portion of Eu^{3+} ions form a secondary phase instead of being part of the calcium fluoride lattice. The extra diffraction peaks observed in Fig. 2(a) can be indexed in the hexagonal EuF_3 crystal structure ($P\bar{3}c1$ space group). At this europium concentration level, [Eu^{3+}] = 5.4 mol%, the diffraction intensity of these planes represents only an 8% of the total intensity, being much weaker than the signal coming from the CaF_2 lattice. Therefore, this minority phase can be neglected at this concentration level. Then, in the present work the Eu^{3+} content has been kept below the 6 mol% concentration limit to avoid the formation of EuF_3 (compare, for instance, the X-Ray patterns of NPs # 5 and # 3 ([Eu^{3+}] = 5.4 mol% and 1.7 mol%), Fig. 2(a) and (b), with that of pure CaF_2, Fig. 2(c)).

The Rietveld refinement allows achieving other relevant structural information such as the lattice parameters, crystallite size and

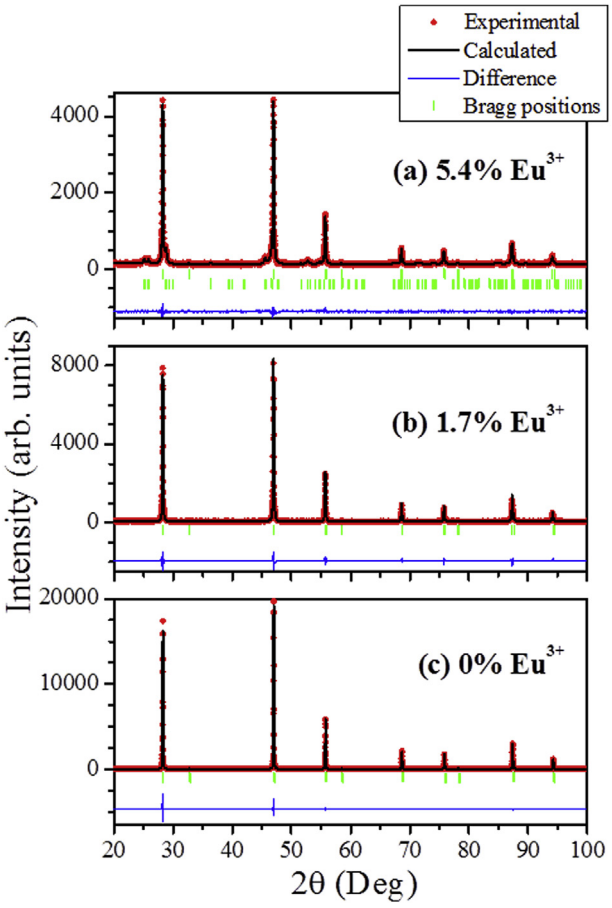

Fig. 2. - Rietveld refinement of XRD patterns corresponding to nanoparticles doped with different Eu^{3+} concentrations.

lattice strain. The angular shift of the diffraction peaks, which has been previously mentioned, is intimately related to modifications in the unit cell dimensions. The evolution of the cubic lattice parameter ($a = b = c$) as function of Eu^{3+} concentration is shown in Fig. 3(a). As it can be observed, the size of the unit cell monotonously increases as Eu^{3+}-doping level increases. Indeed, the volume of the unit cell suffers a progressive dilatation, from a value of 162.92 $(Å)^3$ to 163.45 $(Å)^3$ when the Eu^{3+} concentration changes from 0 to 5.4 mol%. In alkali earth fluorides, this expansion of the unit cell has been also attributed to the charge compensation mechanism previously mentioned [10,16,19,20].

On the other hand, the width of the diffraction peaks provides additional information about the crystallite size and the lattice strain. In particular, the full width at half maximum of the peak profile, FWHM (β_{hkl}), is related to both magnitudes, crystallite size (D) and lattice strain (ε), using the Williamson-Hall relation [8,21]:

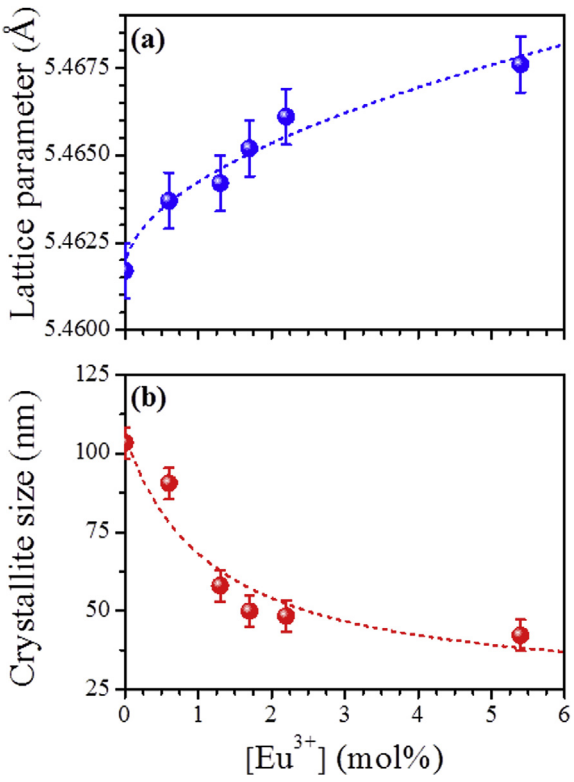

Fig. 3. Evolution of the cubic lattice parameter and crystallite size as function of Eu^{3+} concentration, (a) and (b) respectively. Dashed lines have been included to guide the eye.

$$\beta_{hkl}\cos\theta = \frac{K\lambda}{D} + 4\varepsilon\sin\theta \quad (1)$$

where K is the shape factor ($K = 0.94$ for cubic crystallites), λ is the wavelength of the X-rays ($\lambda = 0.15406$ nm for Cu K_α radiation) and θ is the Bragg diffraction angle.

According to Eq. (1), an average value of the crystallite size and lattice strain can be obtained by making a least squares fitting of $(\beta_{hkl}\cos\theta)$ vs $(\sin\theta)$ using selected (hkl) diffraction peaks. In the present work the most intense diffraction planes: (1 1 1), (2 2 0), (3 1 1), (4 0 0), (3 3 1) and (4 2 2) have been used together with the β_{hkl} values obtained from the Rietveld refinement. The crystallite size, D, is extracted from the intercept value while the lattice strain, ε, is related with the slope of the linear fit.

The results corresponding to the crystallite size (D) as function of Eu^{3+} concentration are presented in Fig. 3(b). As it can be observed, the crystallite size presents a monotonous decrease as Eu^{3+} level increases. This kind of decreasing trend indicates a gradual reduction in the crystallinity and a net rise in the lattice disorder; effect that could be again attributed to the structural distortion provoked by the increasing concentration of interstitial fluorine ions needed to accommodate the Eu^{3+} ions in the cationic positions [10,19].

In relation to the lattice strain (ε), it must be remarked that the linear fits to Eq. (1) give a very small slope values, indicating that in these nanoparticles the lattice strain is negligible ($|\varepsilon| \leq 0.05\%$) at least in the concentration range explored in this work.

The morphology and nanoparticle size distribution have been investigated by analyzing the corresponding SEM micrographs. Representative images of each Eu^{3+} doping level together with its size distributions are presented in Fig. 4. As it can be seen, independently on the Eu^{3+} content, the NPs exhibit the cubic morphology typical of calcium fluoride.

The nanoparticle size distribution was determined by using several SEM micrographs for each Eu^{3+} concentration. It was found that the particle size follows a log-normal distribution being clearly influenced by the doping level (red solid lines in Fig. 4). In fact, the mean particle size evolves from 79 nm to 23 nm when Eu^{3+} concentration changes from 0 mol% to 5.4 mol%.

A summary of the main parameters of the structural analysis (Rietveld refinement) and morphological characterization are presented in Table 1.

3.2. Photoluminescence characterization

The optical properties of the Eu^{3+}-doped CaF_2 NPs have been explored under continuous wave excitation (CW) by using a commercial ultraviolet LED ($\lambda = 401$ nm). As it is depicted in Fig. 5, this pumping scheme excites the europium ions from the ground state to the upper energy levels via the $^7F_0 \rightarrow {}^5L_6$ absorption band, from where the decay is governed by multi-phonon relaxations that finally populate the $^5D_0$ manifold. The $^5D_0 \rightarrow {}^7F_J$ radiative transitions produce the characteristic Eu^{3+} orange-red emission bands in the spectral range 570–720 nm, being particularly interesting those that end in the ^7F_J levels with J = 1, 2 and 4. The first one, $^5D_0 \rightarrow {}^7F_1$ transition, presents a pure magnetic dipole (MD) character and it is practically not influenced by the chemical surroundings of the Eu^{3+} ions. In contrast, the $^5D_0 \rightarrow {}^7F_{2,4}$ transitions have a pure electric dipole (ED) character being, therefore, quite sensitive to the ion environment. This exceptional combination of pure MD- and ED-transitions makes Eu^{3+} ions a perfect spectroscopic probe to investigate the site symmetry in which it is immersed [17,18].

Fig. 6(a) shows the emission spectra of the Eu^{3+}-doped CaF_2 NPs as function of Eu^{3+} doping level after CW excitation at $\lambda_{exc} = 401$ nm. As it can be appreciated, the emission spectra are dominated by the 4f → 4f electronic transitions corresponding to the radiative relaxations from $^5D_0$ manifold to the ^7F_J lower lying levels, with J = 0, 1, 2, 3 and 4, being the most intense those that end in the $^7F_{1,2,4}$ manifolds. The prevalence of the pure MD transition, $^5D_0 \rightarrow {}^7F_1$, over those with a pure ED character, $^5D_0 \rightarrow {}^5F_2$ and $^5D_0 \rightarrow {}^5F_4$, is a clear indicative of the high symmetry at the Eu^{3+} sites in CaF_2 [10,17,18,22]. Finally, as well as in other Eu^{3+}-activated materials [2,5], the intensity of the $^5D_0 \rightarrow {}^7F_0$ and $^5D_0 \rightarrow {}^7F_3$ europium transitions are very weak due to their forbidden character [18].

It is also apparent from this figure that the total emission intensity depends on the europium content. The integrated emission intensity as function of the Eu^{3+} concentration is presented in Fig. 6(b). As it can be seen, in diluted samples ($[Eu^{3+}] \leq 2$ mol%) the intensity increase basically linearly with the doping level, while for higher concentrations it departs from the linear relationship exhibiting the typical saturation behavior associated to the presence of luminescent quenching mechanisms.

On the other hand, as it has been previously mentioned, the relative intensities of the radiative channels from $^5D_0$ manifold to ^7F_J lower lying levels (J = 1, 2, 4) can be used to obtain information about the site symmetry. For that purpose it is usual to define the asymmetry ratio, R, as the quotient between the intensities of the $^5D_0 \rightarrow {}^7F_2$ hypersensitive ED transition (I_{ED}) and the $^5D_0 \rightarrow {}^7F_1$ MD transition (I_{MD}), that is:

$$R = \frac{I_{ED}}{I_{MD}} \quad (2)$$

Fig. 6(c) shows the evolution of the asymmetry ratio with the Eu^{3+} concentration. As it can be seen, this ratio increases progressively as the dopant level grows. Indeed along the concentration

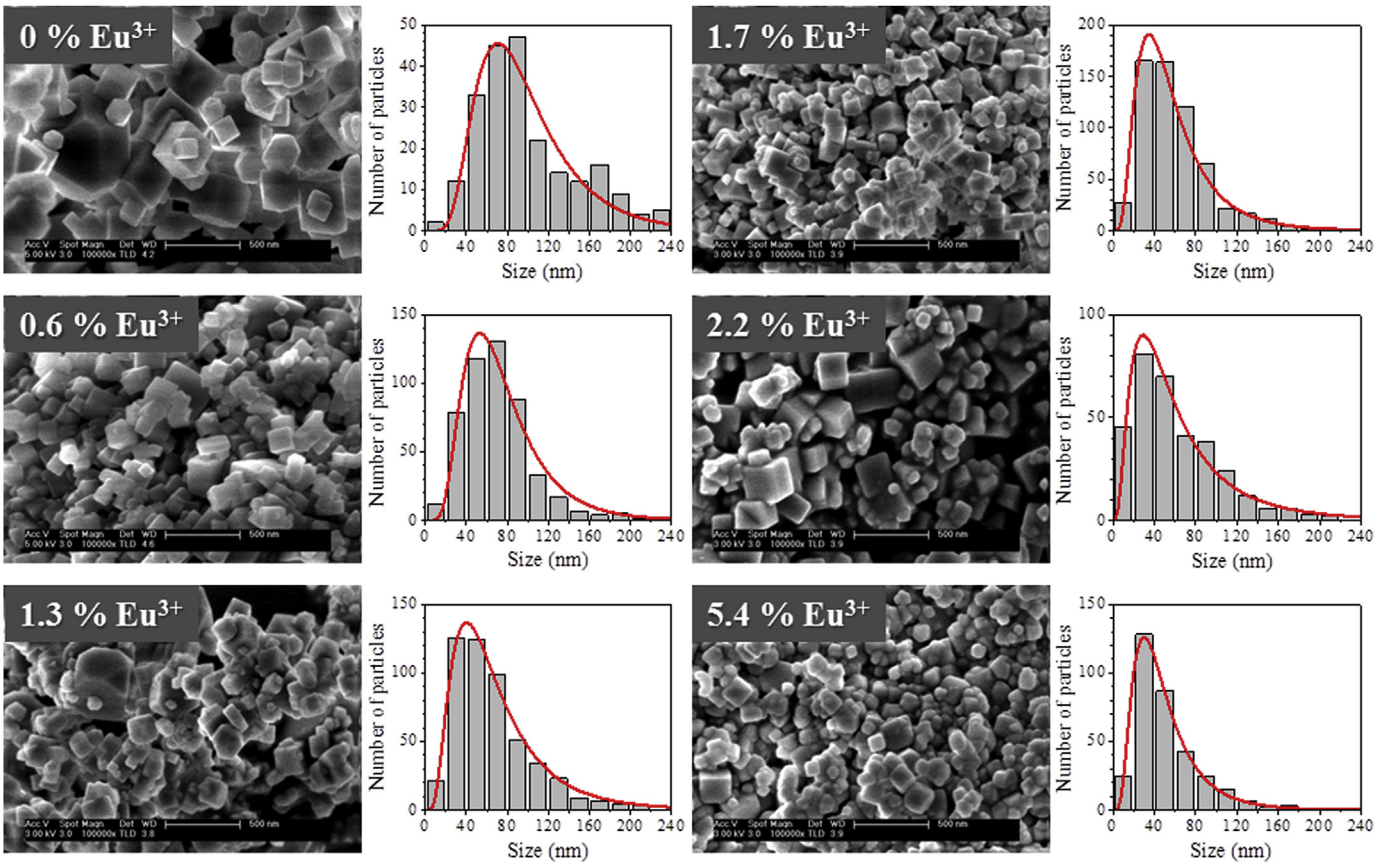

Fig. 4. - SEM micrographs of the CaF_2:Eu^{3+} NPs showing the morphology and nanoparticle size distribution as function of Eu^{3+} concentration (solid red lines represent the fitting to the log-normal distribution). (For interpretation of the references to colour in this figure legend, the reader is referred to the Web version of this article.)

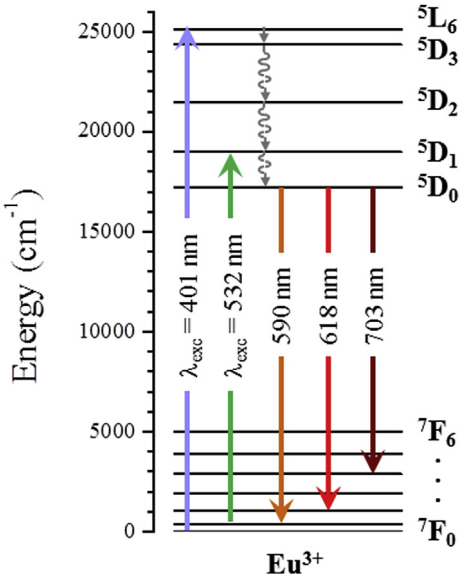

Fig. 5. Partial energy level diagram of Eu^{3+} ions showing the pumping schemes used to perform the CW photoluminescence characterization and to measure the $^5D_0$ luminescent decays.

range explored in this work, the R value experiences a net enhancement of a 65%, changing from $R = 0.40$ to $R = 0.66$ when Eu^{3+} concentration varies from 0.6 mol% to 5.4 mol%. This fact indicates that the ED radiative probabilities of $^5D_0 \rightarrow {}^7F_{2,4}$ Eu^{3+} transitions are favored by the rising dopant level. Considering that in a pure centro-symmetric site these transitions are forbidden, this result indicates that the centro-symmetric character of the europium site in the calcium fluoride nanoparticles decreases as the Eu^{3+} content increases [17,18,22]; being in good accordance with the results obtained from the structural analysis. Then, the reduction in the site symmetry can be associated to the effective increase in the disorder caused by the presence of interstitial fluorine ions.

The spectroscopic characterization previously presented, under CW excitation, gives important information about the population dynamics under steady state conditions, as well as about the local site symmetry of europium ions. Nevertheless, a full characterization of the $^5D_0$ emitting level requires also the study of the population dynamics. For that reason the temporal evolution of the luminescence from the $^5D_0$ level, as function of Eu^{3+} concentration, was measured under pulsed excitation at $\lambda_{exc} = 532$ nm (coincident with the $^7F_1 \rightarrow {}^5D_1$ europium absorption, see energy level diagram of Fig. 5). The luminescent decays of this level, measured at the dominant emission band $^5D_0 \rightarrow {}^7F_1$ ($\lambda_{emi} = 590$ nm), are presented in Fig. 7. As it can be appreciated, within the Eu^{3+} concentration range explored in this work, the temporal decays are complex and cannot be described by a single exponential function, even in the most diluted NPs ([Eu^{3+}] = 0.6 mol%).

In this situation, the luminescent temporal decays are usually characterized by a mean decay time, $<\tau>$, defined as the average value of the temporal intensity distribution, that is:

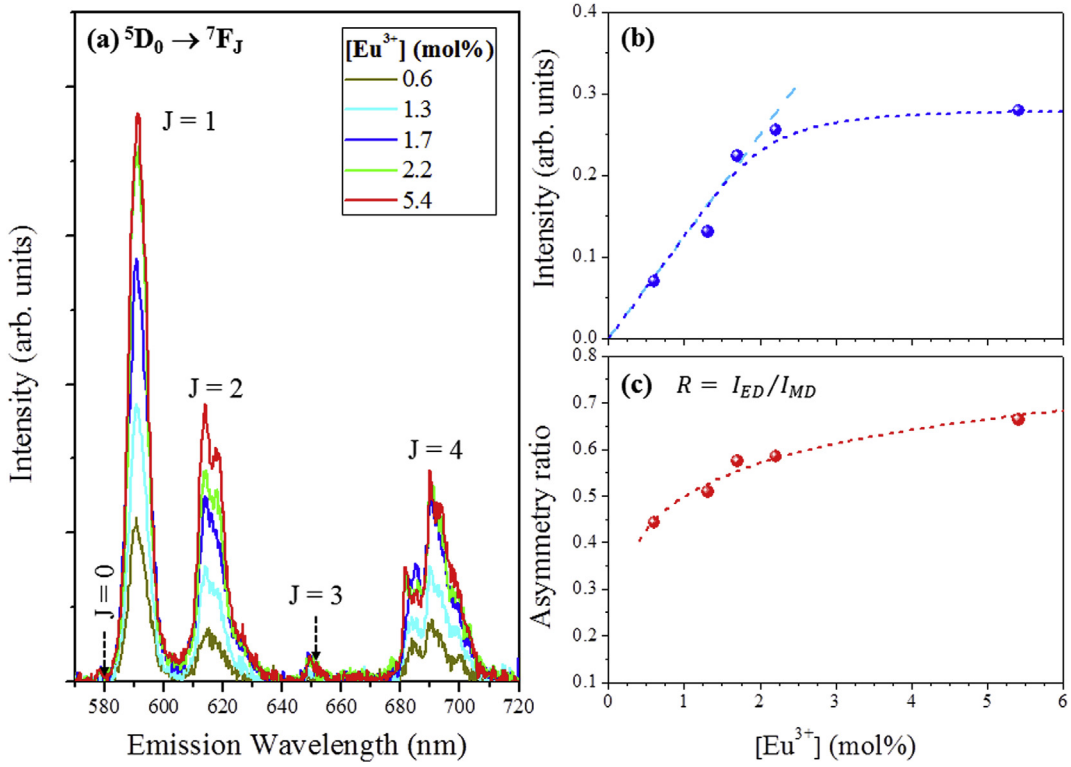

Fig. 6. (a) Emission spectra, (b) integrated emission intensity and (c) asymmetry ratio measured under excitation at $\lambda_{exc} = 401$ nm, as function of Eu^{3+} concentration. Dashed lines were included to guide the eye.

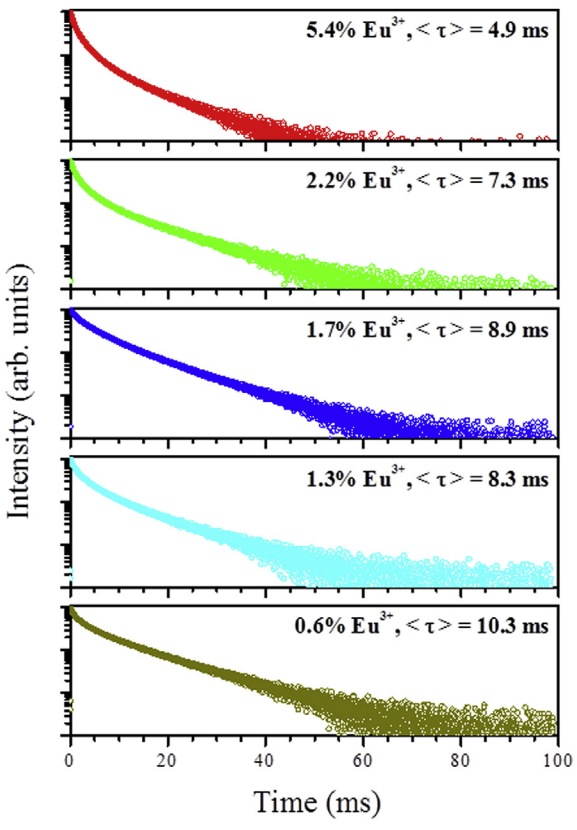

Fig. 7. - Luminescent temporal decays of the $^5D_0$ manifold measured in the CaF_2:Eu^{3+} nanoparticles, under pulsed excitation at $\lambda_{exc} = 532$ nm.

$$<\tau> = \frac{\int tI(t)dt}{\int I(t)dt} \quad (3)$$

The calculated average decay time values have been also included in Fig. 7. As it can be seen, the decay time suffers a strong reduction, from $<\tau> = 10.3$ ms to $<\tau> = 4.9$ ms when Eu^{3+} concentration increases from [Eu^{3+}] = 0.6 mol% to [Eu^{3+}] = 5.4 mol%. This reduction will be discussed in detail later after determining the basic spectroscopic properties of the europium ions in CaF_2 NPs.

3.3. Judd-Ofelt analysis

The theory formulated by Judd and Ofelt [23,24] is generally applied to determine basic spectroscopic properties of Ln^{3+}-doped materials, such as ED transition probabilities, radiative lifetimes and branching ratios, in terms of three intensity parameters, Ω_t ($t = 2, 4, 6$), that can be estimated from the knowledge of the absorption cross sections.

In the particular case of Eu^{3+}-activated materials, it is also possible to apply an alternative Judd-Ofelt (JO) procedure starting from the emission spectrum [17,18,25]. In this modified method, the $^5D_0 \rightarrow {}^7F_1$ MD transition can be used as reference to calibrate the other ED dipole transitions originated in the $^5D_0$ manifold ($^5D_0 \rightarrow {}^7F_{2,4,6}$ transitions). The method takes advantage of the fact that MD transition probabilities can be theoretically evaluated if the energies, eigenvectors and coupling coefficients associated to the intermediate *LS*-coupled states are known [26,27]. In particular, after evaluating the matrix elements of the magnetic-dipole operator and applying the corresponding selection rules in the Russel-Saunders limit, it has been obtained that the $A_{0\rightarrow 1}$ MD transition probability is:

Table 2
Squared reduced matrix elements for $^5D_0 \rightarrow {}^7F_{J'}$ (J' = 2, 4, 6) europium transitions.

Transition $^5D_0 \rightarrow {}^7F_{J'}$	$\lvert\langle 0\lVert U^{(2)}\rVert J'\rangle\rvert^2$	$\lvert\langle 0\lVert U^{(4)}\rVert J'\rangle\rvert^2$	$\lvert\langle 0\lVert U^{(6)}\rVert J'\rangle\rvert^2$
$J'=2$	0.0032	0	0
$J'=4$	0	0.0023	0
$J'=6$	0	0	0.0002

$$A_{0\rightarrow 1} = 14.21\, n_{0\rightarrow 1}^3 \tag{5}$$

where $n_{0\rightarrow 1}$ is de refractive index at $\lambda_{0\rightarrow 1}$. On the other hand, the radiative probabilities ($A_{0\rightarrow J}$) and the integrated emission intensities ($I_{0\rightarrow J}$) are related by [18,22,25]:

$$\frac{A_{0\rightarrow 2,4,6}}{A_{0\rightarrow 1}} = \frac{I_{0\rightarrow 2,4,6}}{I_{0\rightarrow 1}} \frac{\lambda_{0\rightarrow 2,4,6}}{\lambda_{0\rightarrow 1}} \tag{6}$$

where $\lambda_{0\rightarrow J}$ symbolizes the barycenter wavelength of $^5D_0 \rightarrow {}^7F_J$ Eu^{3+} transition ($J = 1, 2, 4, 6$). Then, combining Eqs. (5) and (6), the radiative probability associated to the ED transition can be evaluated by:

$$A_{0\rightarrow 2,4,6} = \frac{I_{0\rightarrow 2,4,6}}{I_{0\rightarrow 1}} \frac{\lambda_{0\rightarrow 2,4,6}}{\lambda_{0\rightarrow 1}} 14.21\, n_{0\rightarrow 1}^3 \tag{7}$$

The radiative probability for the $J \rightarrow J'$ ED transition can be expressed in terms of the JO intensity parameters, $\Omega_t (t = 2, 4, 6)$ and the squared reduced matrix elements, $\lvert\langle J\lVert U^{(t)}\rVert J'\rangle\rvert^2$, as:

$$A_{J\rightarrow J'} = \frac{64\pi^4 e^2}{3h(2J+1)\lambda_{J\rightarrow J'}^3} \frac{n_{J\rightarrow J'}\left(n_{J\rightarrow J'}^2+2\right)^2}{9} \sum_{t=2,4,6} \Omega_t \left|\left\langle J\right|\left|U^{(t)}\right|\left|J'\right\rangle\right|^2 \tag{8}$$

where e is the electron charge, $n_{J\rightarrow J'}$ is de refractive index at the barycenter wavelength ($\lambda_{J\rightarrow J'}$) and h represents the Planck's constant.

The corresponding squared reduced matrix elements of $^5D_0 \rightarrow {}^7F_{J'}$ transitions are presented in Table 2. As it can be seen, the unique non-zero elements are those corresponding to the diagonal elements J' with $t = 2, 4, 6$ [17].

Thus, JO intensity parameters, Ω_t, can be independently determined from the individual transition probabilities:

$$A_{0\rightarrow t} = \frac{64\pi^4 e^2}{3h\left(2J+1\right)\lambda_{J\rightarrow J'}^3} \frac{n_{J\rightarrow J'}\left(n_{J\rightarrow J'}^2+2\right)^2}{9} \sum_{t=2,4,6} \Omega_t \left|\left\langle 0\right|\left|U^{(t)}\right|\left|t\right\rangle\right|^2 \tag{9}$$

The Ω_t parameters are then readily calculated from the integrated emission intensities ($I_{0\rightarrow J}$). In the calculus, the wavelength dependence of the refractive index has been considered by using the dispersion formula previously reported for CaF_2 [28].

It must be noted that the intensity of the $^5D_0 \rightarrow {}^7F_6$ emission band (centered at around 0.8 μm) is too weak to be detected and no information about Ω_6 JO parameter can be obtained from the emission spectrum [22,29–32]. However, the value of Ω_6 is unnecessary to predict the dynamics of the $^5D_0$ emitting manifold because the non-zero element presents a very small value, and its contribution to the overall transition probability is negligible.

This procedure has been applied to determine the JO intensity parameters ($\Omega_{2,4}$), radiative transition probabilities, branching ratios ($\beta_{0\rightarrow J} = A_{0\rightarrow J}/\sum_{J'} A_{0\rightarrow J'}$) and radiative lifetimes ($\tau_R = 1/\sum_J A_{0\rightarrow J}$) as function of Eu^{3+} concentration. These values are summarised in Table 3.

The radiative probabilities of ED transitions present a clear dependence on Eu^{3+} concentration. In particular while the probability ($A_{0\rightarrow 2}$) of the hypersensitive transition, $^5D_0 \rightarrow {}^7F_2$, increases monotonously with the doping level, the probability ($A_{0\rightarrow 4}$) of the $^5D_0 \rightarrow {}^7F_4$ ED-transition remains constant for the lower concentrations and then slightly decreases for the most concentrated NPs. These dependencies are automatically transferred to Ω_2 and Ω_4 parameters, as it is depicted in Fig. 8(a).

The Ω_2 parameter is sensitive to structural changes in the vicinity of the lanthanide ion and to the magnitude of the covalence between Eu^{3+} ion and surrounding ligands (larger values of Ω_2 imply a stronger covalence) [29–34]. The Ω_4 parameter is sensitive to the rigidity of the medium being a long-range effect [30–32,34]. Then, the gradual enhancement of Ω_2 parameter shown in Table 3, and depicted in Fig. 8(a), indicates that the covalence degree of the Eu^{3+} site in CaF_2 increases monotonously with the doping level. Within the doping level explored in this work, $\Omega_2 < \Omega_4$ evidencing that Eu^{3+} ions occupy high symmetry sites in CaF_2.

The ratio Ω_2/Ω_4 follows a monotonous increment with Eu^{3+} content, see Fig. 8(b), implying that the symmetry around the lanthanide ions is decreasing. This is in agreement with the growing trend observed in the asymmetry ratio, Fig. 6(c).

Finally, in relation to the total radiative transition probability ($A_R = \sum_J A_{0\rightarrow J}$) (see Table 3), the JO analysis predicts an initial slight increment ($|\Delta A_R|/A_R \sim 6\%$) when [$Eu^{3+}$] content rises from 0.6 mol % to 1.7 mol%, and then remains basically constant for higher doping levels. This increment in the transition probability could be related with the increment in the lattice distortion implying a reduction in the local symmetry of Eu^{3+} ions. It must be noted that the calculated values are higher than the reported value for bulk samples[34] with very low doping levels ([Eu^{3+}] = 0.05 mol%) where the lattice distortion should be minimum. This dependency is depicted in Fig. 9(a).

The calculated increment in the transition probability implies a similar reduction in the radiative lifetime value, which is reduced from 10.4 ms to 9.8 ms. This reduction is substantially smaller than the reduction observed in the experimental decay times (Fig. 7). As the difference in Eu^{3+} concentration becomes apparent (more remarkable) for heavily doped samples, this fact must be related to the occurrence of concentration quenching processes. The increase in Eu^{3+} concentration and the decrease in the crystallite size, both clearly related effects, contribute to a fast appearance of

Table 3
Radiative transition probabilities ($A_{0\rightarrow J}$), branching ratios ($\beta_{0\rightarrow J}$), radiative lifetimes (τ_R) and JO intensity parameters as function of Eu^{3+} concentration.

[Eu^{3+}] (mol%)	$A_{0\rightarrow 1}$(s^{-1})	$A_{0\rightarrow 2}$(s^{-1})	$A_{0\rightarrow 4}$(s^{-1})	A_R(s^{-1})	$\beta_{0\rightarrow 1}$(%)	$\beta_{0\rightarrow 2}$(%)	$\beta_{0\rightarrow 4}$(%)	τ_R(ms)	$\Omega_2(10^{-20}\,cm^2)$	$\Omega_4(10^{-20}\,cm^2)$
0.6	41.9	19.3	34.7	95.9	43.6	20.2	36.2	10.4	0.73	2.53
1.3	41.9	22.6	35.1	99.6	42.1	22.7	35.2	10.1	0.85	2.57
1.7	41.9	25.3	34.9	102.1	41.0	24.8	34.2	9.8	0.95	2.55
2.2	41.9	25.7	33.6	101.2	41.4	25.4	33.2	9.9	0.97	2.42
5.4	41.9	29.2	30.9	102.0	41.1	28.7	30.3	9.8	1.10	2.26

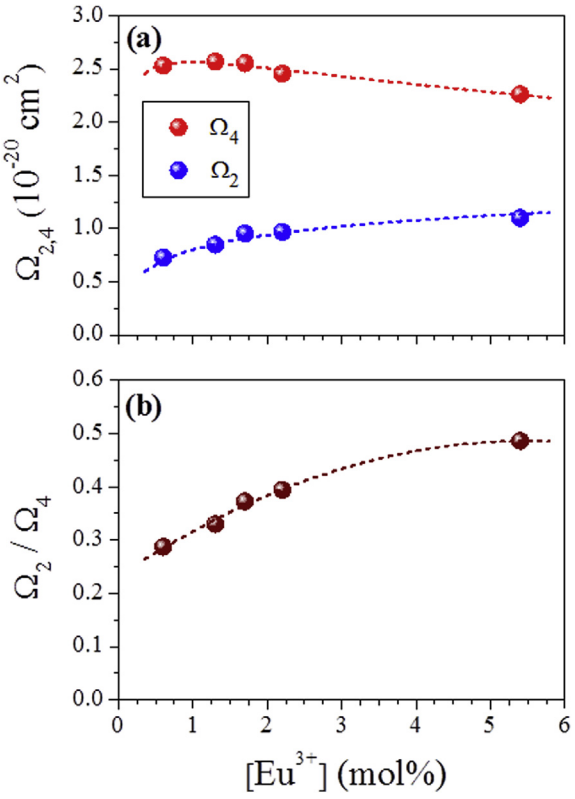

Fig. 8. (a) JO intensity parameters and (b) Ω_2/Ω_4 ratio as function of Eu^{3+} concentration. Dashed lines were included to guide the eye.

concentration quenching mechanisms that strongly reduce the observed decay time. The total de-excitation probability (A_{exp}) could be expressed as the addition of the radiative component (A_R) plus an additional term arising from concentration quenching effects (W_Q):

$$A_{exp} = \frac{1}{<\tau>} = A_R + W_Q \tag{10}$$

From the experimental data it is found that, in this case, this additional term depends linearly with the doping level, a situation

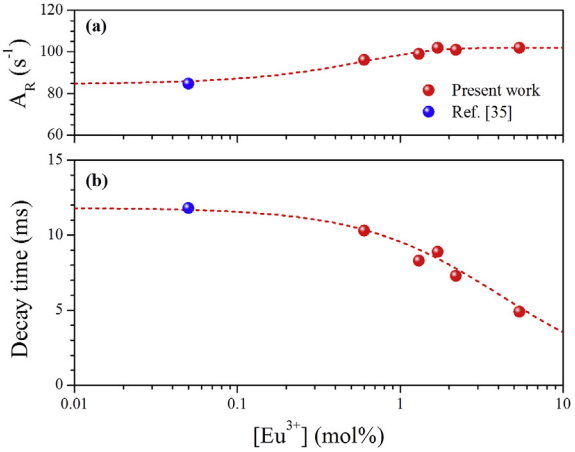

Fig. 9. - (a) Dependence of the radiative transition probability with Eu3+ concentration (dashed line has been drawn to guide the eye). (b) Experimental luminescence decay time corresponding to the $^5D_0$ level measured at $\lambda_{emi} = 590$ nm and the theoretical least squares fitting from eq. (12) (dashed line).

that has also been found in other nanoparticles activated with rare-earth ions [36,37]:

$$W_Q = B\left[Eu^{3+}\right] \tag{11}$$

The overall concentration dependence of the observed decay time can be then described by:

$$<\tau> = \frac{\tau_0}{1 + \tau_0 B\left[Eu^{3+}\right]} \tag{12}$$

where $\tau_0 = 11.8$ ms corresponds to the low concentration lifetime value [35] and $B = 0.020(\text{ms}\cdot\text{mol\%})^{-1}$ is obtained by a least squares fitting of the experimental data as it is depicted in Fig. 9(b).

If we assume that the reported low concentration lifetime value ($\tau_0 = 11.8$ ms) is unaffected by concentration quenching, we could estimate relative luminescence quantum yields (QY_{rel}) using this value as reference. The diluted NPs (0.6 mol%) would give a value $QY_{rel} = <\tau>/\tau_0 \sim 87\%$, which decreases with Eu^{3+} concentration, reaching a value $QY_{rel} \sim 41\%$ for the most concentrated sample (5.4 mol%). These values are higher than those reported for several europium doped alkali fluorides CaF_2, SrF_2 and BaF_2 which range between $25 \leq QY_{rel} \leq 35\%$ depending also on the solvent used [38], although using a higher doping level (10 mol%).

The reduction of quantum yield with concentration is consistent with the dependence of the emitted intensity (Fig. 6(b)). At low concentration the quantum yield remains high and the intensity increases linearly while at higher concentration the reduction in QY counterbalances the increase of emitting centers and the emission intensity saturates. This suggests that, from the practical point of view, the best compromise is obtained for europium concentration around 2 mol%, which is also in accordance with the results reported for SrF_2:Eu^{3+} nanospheres [39].

4. Conclusions

In the present work, Eu^{3+}-doped CaF_2 nanocubes with variable europium concentration were synthesized by a chemical route based on a direct precipitation method at low temperature and pH = 3. The crystalline structure and morphology have been investigated, as function of Eu^{3+} concentration, by means of X-ray Powder Diffraction and Scanning Electron Microscopy, respectively. It has been found that, within the concentration range explored in this work ([Eu^{3+}] < 6 mol%), the structure of the synthesized NPs is coincident with the fluoride-type structure ($Fm\bar{3}m$ space group) exhibiting the typical cubic morphology associated to CaF_2 crystals.

The NP size follows a log-normal distribution whose mean values decrease with europium content, changing from 79 nm to 36 nm when Eu^{3+} varies from 0 to 5.4 mol%.

The Rietveld refinement indicates that Eu^{3+} incorporation produces lattice distortion inducing a lattice parameter increase from 5.4617 Å, for pure CaF_2, to 5.4676 Å when Eu^{3+} concentration reaches the highest doping level (5.4 mol%). In relation to the crystallite size, it follows an opposite trend, decreasing with Eu^{3+} content.

The spectroscopic properties of Eu^{3+} ions have been studied under CW and pulsed excitation. Taking advantage of the sensibility of Eu^{3+} ions to the local chemical environment, it has been possible to detect changes in the luminescence properties, namely emission intensities and decay times.

A modified Judd-Ofelt procedure, based on the emission spectrum, has been used to determine the basic spectroscopic properties (transition probabilities, radiative lifetimes and branching ratios) associated to the $^5D_0$ orange-red emitting level.

It has been found that in these nanocubes the Ω_2 and Ω_4 Judd-

Ofelt intensity parameters present a smooth evolution with the doping level. The Ω_2 /Ω_4 ratio increases with Eu^{3+} concentration. This is in accordance with a reduction in the local symmetry of Eu^{3+} ions as the doping level increases, implying a slight increment in the overall radiative transition probability. The reduction in the decay times at concentrations up to $[Eu^{3+}] \sim 2$ mol% can be accounted for the increase of radiative transition probability. Only above these values the observed lifetime reduction should be linked to concentration quenching effects.

Acknowledgements

This work has been partially supported by Ministerio de Economía y Competitividad and Ministerio de Ciencia, Innovación y Universidades under projects MAT2016-75716-2-2-R and RTI2018-101020-B-I00.

References

[1] P. Ramasamy, P. Manivasakan, J. Kim, Upconversion nanophosphors for solar cell applications, RSC Adv. 4 (2014) 34873–34895.
[2] Y.I. Jeon, L.K. Bharat, J.S. Yu, Eu^{3+} ions co-doped CLPO:Dy^{3+} single phase white-light emitting phosphors for near UV-based white LEDs, J. Alloy. Comp. 649 (2015) 531–536.
[3] H. Groult, J. Ruiz-Cabello, J. Pellico, A.V. Lechuga-Vieco, R. Bhavesh, M. Zamai, E. Almarza, I. Martín-Padura, E. Cantelar, M.P. Martínez-Alcázar, F. Herranz, Parallel multifunctionalization of nanoparticles: a one-step modular approach for in vivo imaging, Bioconjug. Chem. 26 (2015) 153–160.
[4] H.D.A. Santos, E.C. Ximendes, M.C. Iglesias de la Cruz, I. Chaves-Coira, B. del Rosal, C. Jacinto, L. Monge, I. Rubia-Rodríguez, D. Ortega, S. Mateos, J. García Solé, D. Jaque, N. Fernández, In vivo early tumor detection and diagnosis by infrared luminescence transient nanothermometry, Adv. Funct. Mater. 28 (2018) 1803924-1–1803924-10.
[5] M. Laguna, N.O. Núñez, V. Rodríguez, E. Cantelar, G. Stepien, M.L. García, J.M. de la Fuente, M. Ocaña, Multifunctional Eu-doped $NaGd(MoO_4)_2$ nanoparticles functionalized with poly(L-lysine) for optical and MRI imaging, Dalton Trans. 45 (2016) 16354–16365.
[6] D. Sarkar, S. Ganguli, T. Samanta, V. Mahalingam, Design of lanthanide-doped colloidal nanocrystals: application as phosphors, sensors, and photocatalysts, Langmuir 35 (2019) 6211–6230.
[7] P. Ghosh, R.K. Sharma, Y.N. Chouryal, A.V. Mucring, Size of rare-earth ions: a key factor in phase tuning and morphology control of binary and ternary rare-earth fluoride materials, RSC Adv. 7 (2017) 33467–33476.
[8] A.B. Andrade, N.S. Ferreira, M.E.G. Valerio, Particle size effects on structural and optical properties of BaF_2 nanoparticles, RSC Adv. 7 (2017) 26839–26848.
[9] P. Cortelletti, M. Pedroni, F. Boschi, S. Pin, P. Ghigna, P. Canton, F. Vetrone, A. Speghini, Luminescence of Eu^{3+} activated CaF_2 and SrF_2 nanoparticles: effect of the particle size and codoping with alkaline ions, Cryst. Growth Des. 18 (2018) 686–694.
[10] F. Wang, X. Fan, D. Pi, M. Wang, Synthesis and luminescence behavior of Eu^{3+}-doped CaF_2 nanoparticles, Solid State Commun. 133 (2005) 775–779.
[11] W. Ye, X. Liu, Q. Huang, Z. Zhou, G. Hu, Co-precipitation synthesis and self-reduction of CaF_2:Eu^{2+} nanoparticles using different surfactants, Mater. Res. Bull. 83 (2016) 428–433.
[12] B. Zhao, D. Shen, Q. Tan, J. Tang, X. Zhou, S. Hu, J. Yang, Morphology-controllable luminescence properties of Ce^{3+}/Tb^{3+}/Eu^{3+}-doped CaF_2 microcrystals, J. Mater. Sci. 52 (2017) 5857–5870.
[13] M.Y.A. Yagoub, H.C. Swart, E. Coetsee, Energy transfer study between Ce^{3+} and Tb^{3+} ions in a calcium fluoride crystal for solar applications, J. Lumin. 187 (2017) 96–101.
[14] P. Cortelletti, C. Facciotti, I.X. Cantarelli, P. Canton, M. Quintanilla, F. Vetrone, A. Speghini, M. Pedroni, Nd^{3+} activated CaF_2 NPs as coloidal nanothermometers in the biological window, Opt. Mater. 68 (2017) 29–34.
[15] M. Straßer, J.H.X. Schrauth, S. Dembski, D. Haddad, B. Ahrens, S. Schweizer, B. Christ, A. Cubukova, M. Metzger, H. Walles, P.M. Jakob, G. Sextl, Calcium fluoride based multifunctional nanoparticles for multimodal imaging, J. Nanotechnol. 8 (2017) 1484–1493.
[16] R. Wang, M. Yuan, C. Zhang, H. Wang, X. Xu, Tunable multicolor and enhanced red emission of monodispersed CaF_2:Yb^{3+}/Ho^{3+} microspheres via Mn^{2+} doping, Opt. Mater. 79 (2018) 403–407.
[17] R. Reisfeld, E. Zigansky, M. Gaft, Europium probe for estimation of site symmetry in glass films, glasses and crystals, Mol. Phys. 102 (2004) 1319–1330.
[18] K. Binnemans, Interpretation of europium (III) spectra, Coord. Chem. Rev. 295 (2015) 1–45.
[19] G. Zhi, J. Song, B. Mei, W. Zhou, Synthesis and characterization of Er^{3+} doped CaF_2 nanoparticles, J. Alloy. Comp. 509 (2011) 9133–9137.
[20] Y. Jin, Hydrothermal synthesis and luminescent properties of (Sr,Ba)F_2:Eu^{3+} nanostructures, J. Nanosci. Nanotechnol. 16 (2016) 9856–9861.
[21] R. Sivakami, S. Dhanuskodi, R. Karvembu, Estimation of lattice strain in nanocrystalline RuO_2 by Williamson-Hall and size-strain plot methods, Spectrochim, Acta A Mol. Biomol. Spectrosc. 152 (2016) 43–50.
[22] N. Rakov, R.B. Guimaraes, W. Lozano, G.S. Maciel, Structural and spectroscopic analysis of europium doped yttrium oxyfluoride powders prepared by combustion synthesis, J. Appl. Phys. 114 (2013), 043517.
[23] B.R. Judd, Optical absorption intensities of Rare-Earth ions, Phys. Rev. 127 (1962) 750–761.
[24] G.S. Ofelt, Intensities of crystal spectra of Rare-Earth ions, J. Chem. Phys. 37 (1962) 511–520.
[25] M.J. Weber, T.E. Varitimos, B.H. Matsinger, Optical intensities of rare-earth ions in yttrium orthoaluminate, Phys. Rev. B 8 (1973) 47–53.
[26] M.J. Weber, Probabilities for radiative and nonradiative decay of Er^{3+} in LaF_3, Phys. Rev. 157 (1967) 262–272.
[27] E. Cantelar, M. Marin-Dobrincic, T. Jardiel, A.C. Caballero, F. Cussó, Judd-Ofelt analysis of powder samples: $LiNbO_3$:Er^{3+} submicron-sized particles as a model case, Opt. Mater. 41 (2015) 122–125.
[28] I.H. Malitson, A redetermination of some optical properties of calcium fluoride, Appl. Opt. 2 (1963) 1103–1107.
[29] R. Shukla, S.K. Gupta, V. Grover, V. Natarajan, K. Tyagi, The role of reaction conditions in the polymorphic control of Eu^{3+} doped $YInO_3$: structure and size sensitive luminescence, Dalton Trans. 44 (2015) 10628–10635.
[30] M. Ferhi, C. Bouzidi, K. Horchani-Naifer, H. Elhouichet, M. Ferid, Judd-Ofelt analysis of spectroscopic properties of Eu^{3+} doped $KLa(PO_3)_4$, J. Lumin. 157 (2015) 21–27.
[31] I. Ahemen, O. Meludu, F.B. Dejene, B. Viana, Site spectroscopy of Eu^{3+} doped-ZnS nanocrystals embebbed in sodium carbosymethyl cellulose matrix, Opt. Mater. 61 (2016) 82–91.
[32] I. Ahemen, F.B. Dejene, R.E. Kroon, H.C. Swart, Effect of europium ion concentration in the structural and photoluminescence properties of novel Li_2BaZrO_4:Eu^{3+} nanocrystals, Opt. Mater. 74 (2017) 58–66.
[33] Y. Nageno, H. Takebe, K. Morinaga, T. Izumitani, Effect of modifier ion son fluorescence and absorption of Eu^{3+} in alkali and alkaline earth silicate glasses, J. Non-Cryst. Solids 169 (1994) 288–294.
[34] J.C. Batista, P.C. de Sousa Filho, O.A. Serra, Effect of the vanadium (v) concentration on the spectroscopic properties of nanosized europium-doped yttrium phosphates, Dalton Trans. 41 (2012) 6310–6318.
[35] J.P.R. Wells, R.J. Reeves, Polarized laser selective excitation and Zeeman infrared absorption of C_{4v} and C_{3v} symmetry centers in Eu^{3+}-doped CaF_2, SrF_2 and BaF_2 crystals, Phys. Rev. B 64 (2001) 035102-1–035102-10.
[36] F. Vetrone, J.C. Boyer, J.A. Capobianco, A. Speghini, M. Bettinelli, Concentration-dependent near-infrared to visible upconversion in nanocrystalline and bulk Y_2O_3:Er^{3+}, Chem. Mater. 15 (2003) 2737–2743.
[37] M. Quintanilla, N.O. Núñez, E. Cantelar, M. Ocaña, F. Cussó, Energy transfer efficiency in YF_3 nanocrystals: quantifying the Yb^{3+} to Tm^{3+} infrared dynamics, J. Appl. Phys. 113 (2013) 174308-1–174308-6.
[38] B. Ritter, P. Haida, F. Fink, T. Krahl, K. Gawlitza, K. Rurack, G. Scholz, E. Kemnitz, Novel and easy acces to highly luminescent Eu and Tb doped ultra-small CaF_2, SrF_2 and BaF_2 nanoparticles – structure and luminescence, Dalton Trans. 46 (2017) 2925–2936.
[39] Y. Jin, W. Qin, J. Zhang, Preparation and optical properties of SrF2:Eu3+ nanospheres, J. Fluor. Chem. 129 (2008) 515–518.